Neuron
Article

Functional Specialization of Seven Mouse Visual Cortical Areas

James H. Marshel,[1,2,3] Marina E. Garrett,[1,2,3] Ian Nauhaus,[1] and Edward M. Callaway[1,2,*]
[1]Systems Neurobiology Laboratories, The Salk Institute for Biological Studies, La Jolla, CA 92037, USA
[2]Neurosciences Graduate Program, University of California San Diego, La Jolla, CA 92037, USA
[3]These authors contributed equally to this work
*Correspondence: callaway@salk.edu
DOI 10.1016/j.neuron.2011.12.004

SUMMARY

To establish the mouse as a genetically tractable model for high-order visual processing, we characterized fine-scale retinotopic organization of visual cortex and determined functional specialization of layer 2/3 neuronal populations in seven retinotopically identified areas. Each area contains a distinct visuotopic representation and encodes a unique combination of spatiotemporal features. Areas LM, AL, RL, and AM prefer up to three times faster temporal frequencies and significantly lower spatial frequencies than V1, while V1 and PM prefer high spatial and low temporal frequencies. LI prefers both high spatial and temporal frequencies. All extrastriate areas except LI increase orientation selectivity compared to V1, and three areas are significantly more direction selective (AL, RL, and AM). Specific combinations of spatiotemporal representations further distinguish areas. These results reveal that mouse higher visual areas are functionally distinct, and separate groups of areas may be specialized for motion-related versus pattern-related computations, perhaps forming pathways analogous to dorsal and ventral streams in other species.

INTRODUCTION

Specialized neural circuits process visual information in parallel hierarchical streams, leading to complex visual perception and behavior. Distinct channels of visual information begin in the retina and synapse through the lateral geniculate nucleus to primary visual cortex (V1), forming the building blocks for visual perception (Nassi and Callaway, 2009). In primates, these information channels are transformed and integrated multiple times over, through increasingly higher-order computations at each stage in a complex hierarchy of extrastriate visual areas that each contain a discrete visuotopic representation of space (Felleman and Van Essen, 1991; Orban, 2008; Van Essen, 2003).

Strikingly, neurons in each of these areas are selective for specific features of a visual stimulus within their receptive fields. In most cases, visual areas represent at least some information along basic feature dimensions such as direction, orientation, spatial frequency, and temporal frequency (Felleman and Van Essen, 1987; Orban, 2008). Differences in the ranges of parameters represented by each population and/or the fraction of neurons selective for particular stimulus attributes functionally distinguish different areas (Baker et al., 1981; Felleman and Van Essen, 1987; Foster et al., 1985; Payne, 1993). Selective feedforward and feedback projections link together areas with related feature selectivities to form parallel processing streams and define hierarchical relationships (Felleman and Van Essen, 1991). Two major parallel processing pathways have been defined based on functional specializations, patterns of connections, and associations with different behaviors. The dorsal pathway is specialized to process motion and spatial relationships and is related to behaviors involving visually guided actions. The ventral pathway is specialized to process fine-scale detail, shapes, and patterns in an image to support object recognition and is associated with visual perception (Maunsell and Newsome, 1987; Ungerleider and Mishkin, 1982; Van Essen and Gallant, 1994).

This wealth of information about the visual system has resulted from decades of research primarily in primate and carnivore species. However, large gaps in understanding remain, most notably relating circuit-level mechanisms and gene expression to specific neuron response characteristics and high-order extrastriate computations. The main limitation preventing this level of understanding is the inaccessibility of these species to large-scale, high-throughput studies relating response characteristics to specific circuit elements or circuit development to specific genes.

The last decade has seen enormous advances along this front in terms of molecular and genetic methods available to understand circuit structure and function at the level of specific genes, well-defined neuronal populations, specific cell types, and single neurons in the mouse (Arenkiel and Ehlers, 2009; Luo et al., 2008). These include methods for identifying connectivity and manipulating or monitoring activity or gene expression across all of these levels. By combining methods for targeting defined cell populations and networks with techniques for monitoring or manipulating activity, it is possible to identify the functions of particular circuit components or specific genes and directly test causal relationships on circuit function and behavior. While these approaches have allowed important insight into numerous neural systems, their use in studies of the mouse visual system has been limited primarily to the mechanisms that generate

orientation selectivity in V1. This is due to a historical reliance on species other than mice, technical limitations, and a lack of knowledge about fundamental properties of mouse visual areas beyond V1.

In order to combine the power of mouse genetics with the advantages of the visual system as a model for understanding mechanisms of brain function, we must obtain an understanding of the mouse visual system that rivals that of more traditional primate and carnivore models. Recent observations indicate that the mouse visual system is surprisingly sophisticated. Behavioral studies indicate that mice can perform complex, visually guided behaviors (Prusky and Douglas, 2004). Functional studies demonstrate that neurons in mouse V1 are highly tuned for visual features such as orientation and spatial frequency, despite the overall lower spatial resolution of the system (Dräger, 1975; Gao et al., 2010; Kerlin et al., 2010; Niell and Stryker, 2008). Furthermore, anatomical experiments reveal that mouse V1 is surrounded by at least nine other cortical regions that receive topographically organized input from V1 (Wang and Burkhalter, 2007). However, despite some preliminary work (Tohmi et al., 2009; Van den Bergh et al., 2010), the functions of mouse extrastriate visual areas are largely unidentified. As a result, answers to the most basic and fundamental questions about mouse visual cortical organization remain unknown. Is each cortical area specialized for extracting information about particular types of features in the visual world? Are increasingly complex representations built up within a hierarchy of visual areas? Are there relatively independent sets of visual areas comprising distinct pathways that carry information related to processing motion versus shape, or specialized for behavioral action versus perception as in the primate visual system?

To establish the mouse as a model for visual information processing, we sought to assess the functional organization of mouse visual cortex. We developed a high-throughput method for characterization of response properties from large populations of neurons in well-defined visual cortical areas. First, we determined the fine-scale retinotopic structure of ten visual cortical areas using high-resolution mapping methods to outline precise area boundaries (Figures 1 and 2). We then targeted seven of these visual areas—primary visual cortex (V1), lateromedial area (LM), laterointermediate area (LI), anterolateral area (AL), rostrolateral area (RL), anteromedial area (AM), and posteromedial area (PM)—for in vivo two-photon population calcium imaging to characterize functional responses of hundreds to thousands of neurons in each area. This allowed us to determine selectivity for fundamental visual features including orientation, direction, spatial frequency, and temporal frequency of defined neural populations in each area, under the same carefully controlled conditions (Figure 3). Comparison of tuning properties across areas revealed that higher visual areas in the mouse encode unique combinations of spatiotemporal information that are distinct from V1 (Figures 4–8). Furthermore, we found that each extrastriate area could be distinguished from every other visual area based on specific combinations of visual feature representations (Figure 7). Together with anatomical information (Berezovskii et al., 2011; Coogan and Burkhalter, 1993; Wang and Burkhalter, 2007), these results suggest that mouse visual cortical areas may comprise hierarchically organized parallel pathways, perhaps similar to the dorsal and ventral streams suggested in other species. This study provides a fundamental understanding of the basic tuning properties of the majority of mouse visual cortical areas using high-throughput methods, laying a foundation for the use of the mouse as a genetically tractable model of visual information processing.

RESULTS

Fine-Scale Retinotopic Mapping of Mouse Visual Cortex Reveals Nine Mouse Visual Areas

Our first goal was to efficiently and precisely map the retinotopic organization of mouse striate and extrastriate visual cortex in order to rapidly target distinct visual areas for population imaging and analysis. Previous anatomical work in mice predicts the existence of at least nine extrastriate visual cortical areas, based on topographic projections from V1 (Olavarria and Montero, 1989; Wang and Burkhalter, 2007). However, functional studies have not identified several detailed features of the retinotopic maps predicted by anatomy, resulting in significant variation between proposed schemes for the areal organization of mouse visual cortex (Kalatsky and Stryker, 2003; Schuett et al., 2002; Wagor et al., 1980; Wang and Burkhalter, 2007). Given the extremely small size of some proposed extrastriate visual areas ($\leq$500 μm), we reasoned that insufficient resolution of previous recording methods, in combination with stimulation of only portions of the visual field in some studies, resulted in incomplete functional retinotopic maps. Thus, to rapidly and reliably target any given visual area in each animal, we developed a fast, sensitive, high-resolution functional recording method to map the retinotopic organization of cortex corresponding to the complete visual hemifield.

We adopted a two-step approach that provided sufficient resolution to reliably define the extent and organization of each cortical visual area rapidly in each animal. First, we used intrinsic signal imaging to measure the hemodynamic response across the visual cortex to drifting bar stimuli at moderate resolution (estimated previously to be on the order of 200 μm (Polimeni et al., 2005)). This was adapted from a sensitive method used previously (Kalatsky and Stryker, 2003), with the key difference that we used a larger stimulus that mapped the entire known visual hemifield of the mouse (Wagor et al., 1980) in spherical coordinates (Supplemental Experimental Procedures, available online). Second, we used low-magnification two-photon calcium imaging to measure the retinotopic organization of visual cortex at high resolution. This resulted in a retinotopic map which was continuous within the extent of visual cortex and allowed us to precisely define borders between several areas based on visual field sign reversals at peripheral representations (Sereno et al., 1995; Figures 1 and 2).

A representative intrinsic imaging map from one animal is shown in Figure 1. Several features of previous map schema are present in the map (for a direct comparison, see Wagor et al., 1980, Figure 4, and Wang and Burkhalter, 2007, Figure 10). Our data are most consistent with the map predicted primarily from anatomy by Wang and Burkhalter (2007), and thus all further analyses and discussion are made in reference to their schema

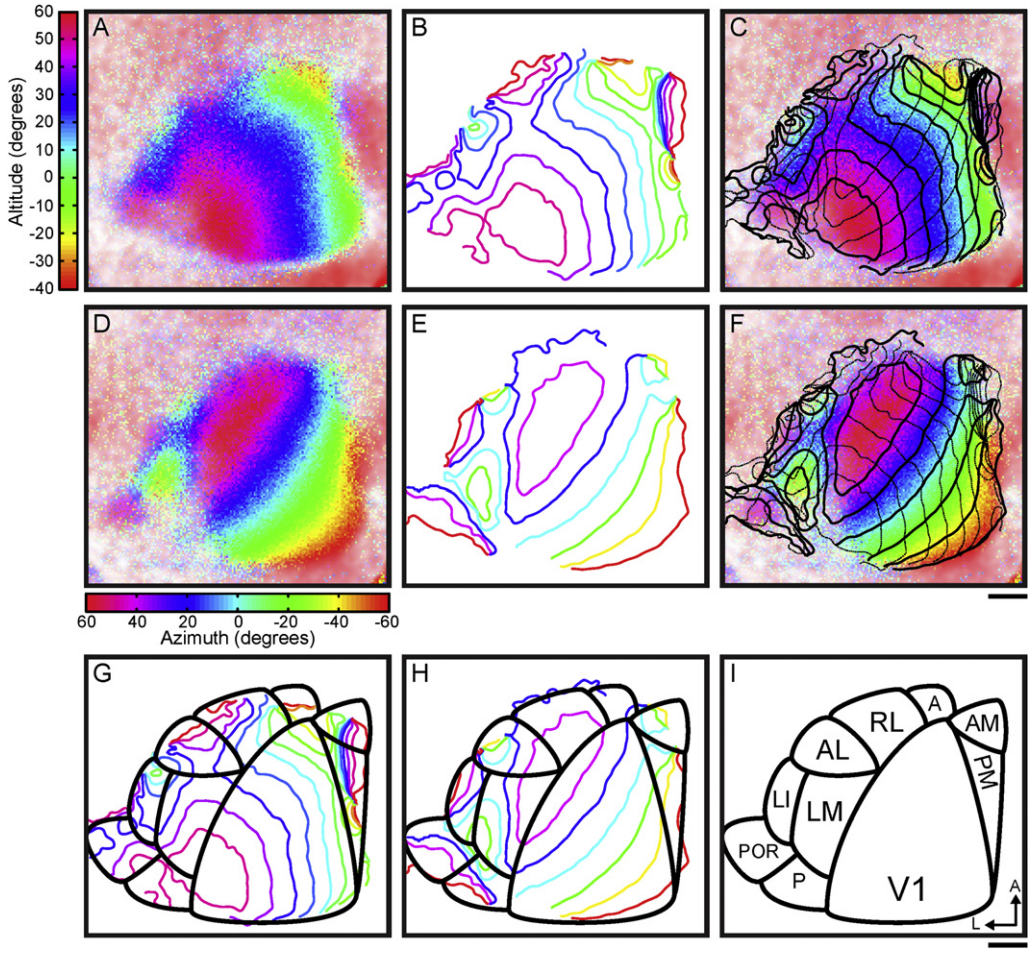

Figure 1. Retinotopic Organization of Mouse Visual Cortex Measured with Intrinsic Signal Imaging

Retinotopic organization of cortex mapped in spherical coordinates. Colors indicate angular position in degrees of a drifting bar stimulus that elicited a hemodynamic response at each cortical location (Figure S1 and Movie S1 and S2).

(A) Continuous vertical retinotopy map. Positive values above the horizontal meridian, located at ~20° altitude (blue), indicate the upper visual field.

(B) Contour lines of vertical eccentricity, with 10° spacing.

(C) Overlay of continuous vertical retinotopy map (as in A) with altitude contours (solid lines, as in B) and azimuth contours (dashed lines, as in E).

(D) Continuous horizontal retinotopy map. Positive values indicate the nasal visual field and negative values the temporal visual field, with the vertical meridian located at ~60° azimuth (purple-red).

(E) Contour lines of horizontal eccentricity with 20° spacing.

(F) Overlay of continuous horizontal retinotopy map (as in D) with azimuth contours (solid lines, as in E) and altitude contours (dashed lines, as in B).

(G) Overlay of vertical retinotopy contour lines (as in B) with area borders (black lines, as in I).

(H) Overlay of horizontal retinotopy contour lines (as in E) with area borders (black lines, as in I). V1 borders extrastriate areas LM, AL, and RL laterally at a reversal at the vertical meridian (purple-red). LI borders LM laterally at a reversal at the temporal periphery (green-yellow). Areas AM and PM border V1 medially at a reversal at the temporal periphery (green-yellow).

(I) Area border diagram of mouse visual cortex. Borders determined based on reversals at peripheries in the vertical and horizontal maps, taking into account high-resolution mapping data (Figure 2 and Figure S2), and correspondence with previous descriptions of areal organization in mouse visual cortex (Wagor et al., 1980; Wang and Burkhalter, 2007). All panels are the same scale; scale bars represent 500 μm.

and area names. Intrinsic imaging maps were sufficient to detect activation in V1, LM, LI, AL, RL, A, AM, PM, P, and POR, but often could not resolve fine-scale details in the maps of relatively small areas (such as LI, RL, A, AM, and PM) that were necessary to precisely define area boundaries.

Using the intrinsic imaging maps as a guide, several calcium dye loadings were performed to load a volume of cortex spanning several millimeters and encompassing several visual areas (Experimental Procedures). We then systematically imaged the extent of the loaded area by moving the objective in ~500–700 μm steps to tile the whole loaded region. At each position, we displayed the retinotopic mapping stimulus (identical to that used for intrinsic imaging) to the animal, and mapped the retinotopy of that ~800–1000 μm^2 patch of cortex with a 16× objective. Mosaics of these individual maps resulted in a complete high-resolution map of the region, often spanning

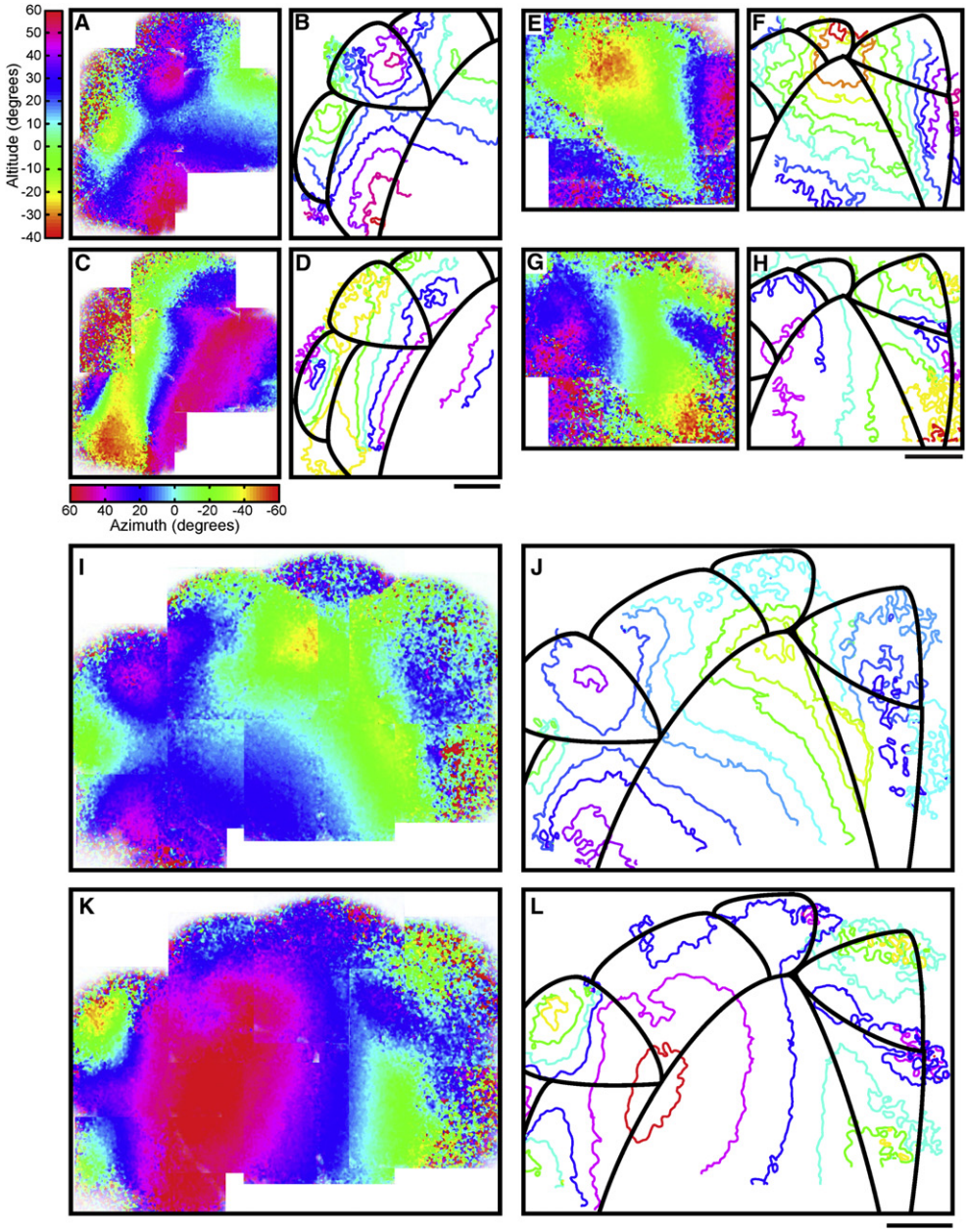

Figure 2. Fine-Scale Retinotopic Organization of Mouse Visual Cortical Areas, Measured with Two-Photon Calcium Imaging

(A–L) Representative high-resolution retinotopic maps of mouse visual cortex. Area borders and names correspond to diagram in Figure 1I. Colors represent retinotopic eccentricity as described in Figure 1. Panels (A), (E), and (I) show continuous vertical retinotopy maps, in altitude coordinates. Panels (B), (F), and (J) show the corresponding contour plots of vertical retinotopy with area borders outlined in black. Panels (C), (G), and (K) show continuous horizontal retinotopy maps, in azimuth coordinates. Panels (D), (H), and (L) show contour plots of horizontal retinotopy, overlaid with area borders.

(A–D) Retinotopic organization of lateral extrastriate areas and their borders with V1. Area borders shown in (B) and (D) correspond to V1, LM, LI, AL, and RL (starting at bottom right, moving clockwise). A reversal at the vertical meridian (nasal periphery, ~60°, purple-red in C and D) delineates the border between V1 and extrastriate areas LM, AL, and RL. A reversal at the temporal periphery (yellow, C and D) marks the border between LM and LI. The border between LM and AL is identified at the reversal near the horizontal meridian (~20°, blue in A and B). AL is separated from RL by a representation of the vertical meridian, extending lateral and anterior from the vertical meridian in V1 (purple-blue, C and D, see also Figure S2E–S2H).

(E–H) Retinotopic organization of anterior and medial extrastriate areas and their borders with V1. Area borders shown in (F) and (H) correspond to V1, LM, AL, RL, A, AM, and PM (starting at lower left, moving clockwise). The border between V1 and PM is identified by a reversal at the temporal periphery (green-yellow, E and F). A representation near the vertical meridian marks the border between AM and PM (blue-purple, G and H).

(I–L) Retinotopic organization of seven visual areas along the nearly entire medial-lateral extent of the visual cortex. Areas shown include LM, AL, RL, A, AM, PM, and V1 (starting from lower left, moving clockwise). All scale bars represent 500 μm. See also Figure S2 for high-resolution maps of P, POR, and the ring-like structure of area RL.

Table 1. Numbers of Neurons Sampled by Cortical Area

	Total Neurons		Responsive and Reliable		Expts	
Area	SF: n	TF: n	SF: n (% Total)	TF: n (% Total)	SF: n	TF: n
V1	1419	1382	728 (51%)	586 (42%)	11	10
LM	590	584	300 (51%)	171 (29%)	7	7
LI	182	193	42 (23%)	23 (12%)	2	2
AL	890	918	330 (37%)	257 (28%)	6	6
RL	616	555	201 (33%)	96 (17%)	6	6
AM	404	311	63 (16%)	12 (4%)	6	6
PM	508	506	147 (29%)	50 (10%)	3	3
Total	4609	4449	1811 (39%)	1195 (27%)	41	40

Total number (n) of neurons recorded in spatial frequency (SF) and temporal frequency (TF) experiments for each cortical area. Number (n) and percent of total of neurons that met criteria for responsiveness ($\Delta F/F > 6\%$) and reliability ($\delta > 1$, Experimental Procedures) and were included in population analysis. Number of fields of view recorded for each area ("Expts"). See Table S1 for additional population criteria.

several millimeters and encompassing the full visuotopic extent of several extrastriate visual areas (Figure 2 and Figure S2). At this resolution, we observed several features in the maps that were not seen with intrinsic imaging, revealing the fine-scale organization of each of eight extrastriate visual areas predicted previously (LM, LI, AL, RL, AM, PM, P, and POR; Figure 2 and Figure S2). We observed some retinotopic structure in the putative location of area A, but did not target this area for population analysis because its retinotopic map was ambiguous in relation to its predicted organization (Wang and Burkhalter, 2007; Figure 2 and Figure S2). It was also difficult to obtain complete maps of areas P and POR given their cortical location (Figure S2). Using this method, we located the region of cortex representing the central visual field within each confidently identified area (~0 degrees azimuth, ~20 degrees altitude) for further analysis. Within this region, we targeted a ~200–300 μm^2 field of view with a 40× objective to characterize visual response properties of populations of neurons at cellular resolution.

Response Characterization and Population Analysis of Neural Populations in Seven Visual Areas

In all, we recorded from over 4,000 neurons, with populations ranging from hundreds to thousands of neurons from each of seven visual areas (V1, LM, LI, AL, RL, AM, PM; Table 1). Two-photon calcium imaging permits recording of neural activity with single cell resolution simultaneously from populations of hundreds of neurons in a given field of view (Figure 3A, left panel). Importantly, tuning curves generated from Oregon Green Bapta-1 AM fluorescence are comparable to those recorded with traditional electrophysiological techniques in mouse visual cortex (Kerlin et al., 2010; Nauhaus et al., 2011). We repeated the retinotopy stimulus to measure the eccentricity represented by each neuron in the 40× field of view and restricted analyses to neurons representing eccentricities within 50° of the center of space so as to match eccentricities across areas. Next, we presented drifting grating stimuli that varied across five spatial frequencies, ranging from 0.01–0.16 cycles per degree (cpd), and eight directions (SF experiment), or five temporal frequencies, ranging from 0.05 to 8 Hz, and eight directions (TF experiment). Responses were measured as the average change in the fluorescence of the calcium dye during the stimulus period across multiple trials, relative to the baseline fluorescence during the prestimulus period (Figure 3A and Figure S3; Experimental Procedures). Mean response magnitude was similar across areas (11%–13% $\Delta F/F$, ANOVA n.s.).

Two-photon calcium imaging provides the unique advantage of being able to quantify the fraction of neurons in a cortical region that reliably respond under a given stimulus condition. Across the entire population of cells from all visual areas, 39% (n = 1,811/4,609) of neurons in the SF experiments, and 27% (n = 1,195/4,449) of neurons in the TF experiments were reliably responsive to at least one stimulus condition (Table 1; Experimental Procedures). Areas differed in the proportion of neurons that responded robustly and reliably to at least one stimulus condition (see Table 1). Intriguingly, in areas with lower proportions of responsive cells (such as AM), responsive neurons were generally extremely robust and selective (Figure 3B and Figure S3F). This demonstrates that neurons in extrastriate visual areas are highly selective for the appropriate stimulus, and suggests that the neurons that did not respond likely require stimuli or other conditions not explored in this study. That a higher fraction of neurons responded during the SF experiment suggests that neurons may be more selective to the appropriate SF than they are to TF within the ranges we tested. Indeed, SF bandwidth tuning was generally sharper than TF bandwidth tuning over the four octaves we sampled in each domain (Figures S4 and S5).

For each reliably responsive neuron, we computed a tuning curve for spatial frequency (SF), temporal frequency (TF), direction, and orientation. For SF and TF, the tuning curves were taken at the direction that gave the maximal response (orange and magenta boxes Figure 3A, Figure S3). For orientation and direction, the tuning curves were taken at the SF that gave the maximal response (yellow boxes Figure 3A, Figure S3). From these tuning curves, we determined tuning and selectivity metrics including the preferred spatial or temporal frequency (pref. SF, pref. TF), spatial and temporal frequency selectivity bandwidth (BW) and low and high cutoffs (LC and HC), and orientation and direction selectivity indices (OSI and DSI).

We compared the population distributions of these tuning metrics across areas to determine whether mouse visual areas encode distinct combinations of visual features. We found that overall, there was a main effect of area on our four primary dependent variables: preferred SF, preferred TF, OSI and DSI, meaning that at least one visual area could be distinguished from another based on scores on these metrics (one-way MANOVA, independent variable: Area, $F_{(24,\ 2537)} = 18.021$, $p < 0.0005$, Wilk's $\lambda = 0.577$, $\varepsilon^2 = 0.128$). We followed up this multivariate test with both parametric and nonparametric univariate tests (both one-way ANOVA and Kruskal-Wallis tests) comparing the scores on each dependent variable as a function of area to determine whether the mean and/or medians could be distinguished statistically in each comparison. Both parametric and nonparametric one-way tests gave comparable results in all instances, and we have shown the

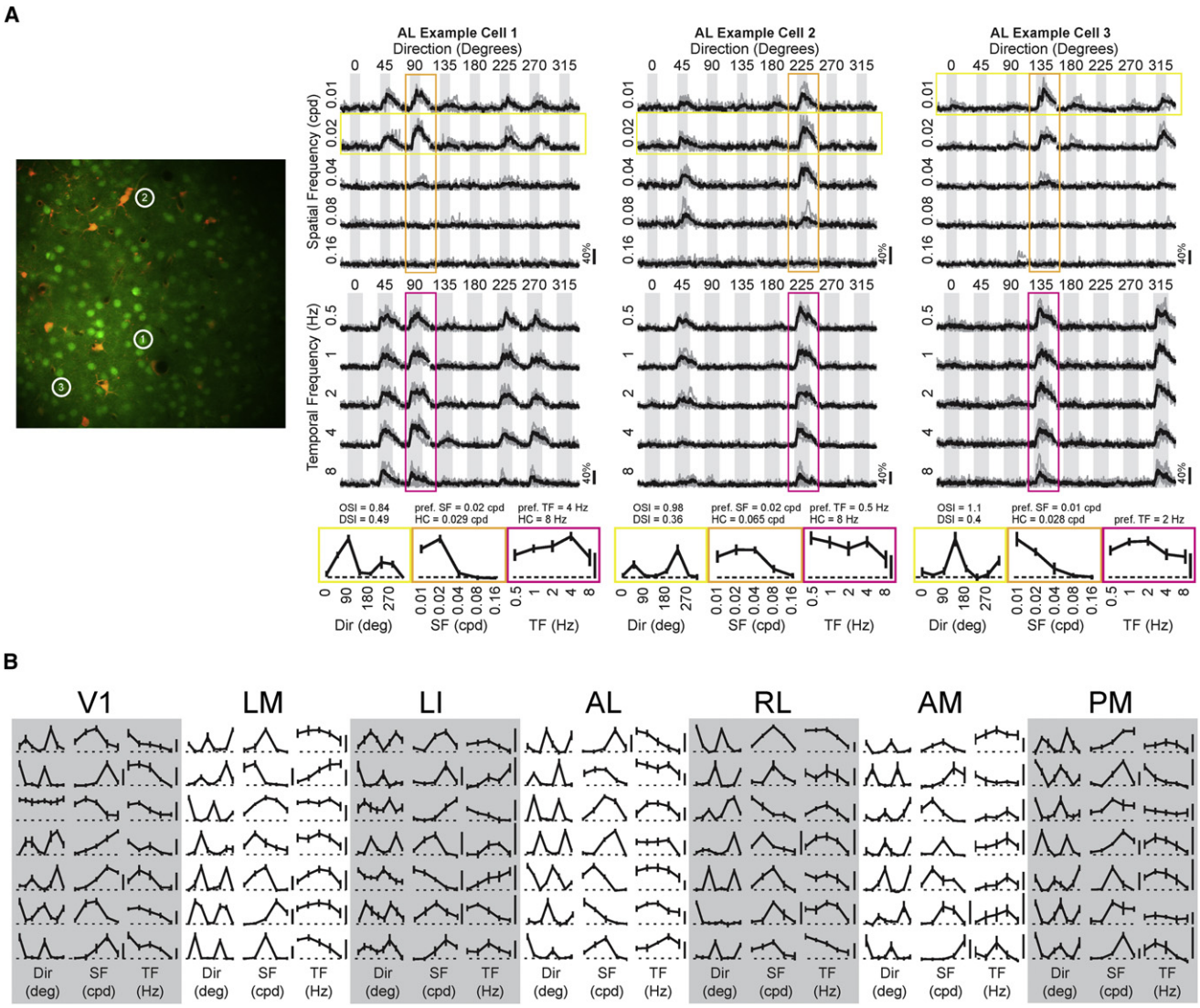

Figure 3. Neurons in Higher Visual Areas Are Selective for Particular Stimulus Features

(A) Example calcium imaging experiment in area AL. Left panel, example two-photon field of view (312 μm × 312 μm). Right panels show three highly responsive neurons, displayed as a matrix of all stimulus conditions for a given experiment. Columns indicate the direction/orientation of the drifting grating, and rows designate the spatial frequency (SF, upper matrices) or temporal frequency (TF, lower matrices). Gray boxes illustrate the duration of the stimulus, 2 s for SF experiments and 4 s for TF experiments. The average response across all trials of a given stimulus condition is shown in black, with the responses to each trial in gray. Scale bar to lower right of each response matrix indicates 40% ΔF/F. Tuning curves were generated from response matrices by computing the average ΔF/F over the two second window following the stimulus onset for each condition along the relevant stimulus dimension. Orientation tuning curves (yellow) are taken at the optimal SF. SF (orange) and TF (magenta) tuning curves are taken at the preferred direction. Values describing selectivity metrics (OSI, DSI), the preferred spatial and temporal frequencies (pref. SF, pref. TF), as well as low cutoff (LC) and high cutoff (HC) frequencies, are listed above the corresponding tuning curves. Scale bars indicate 20% ΔF/F, and correspond to all tuning curves for a given cell.

(B) Representative tuning curves from each visual area demonstrate the diversity and selectivity of receptive field properties across the populations. Horizontal axes are identical to corresponding tuning curves shown in (A), orientation/direction (yellow in A, first column in B), SF (orange in A, second column in B), and TF (magenta in A, third column in B). Scale bars represent 20% ΔF/F and correspond to the set of tuning curves for a given cell. Rows with one scale bar show Dir, SF, and TF tuning curves taken from the same neuron, as in (A). In some cases, the Dir and SF tuning curves are from one neuron, but the TF tuning curve is from a different neuron, indicated by the presence of a scale bar between the SF and TF curves. Example responses from neurons in each area are displayed in Figure S3.

results of the ANOVA tests here. We followed up each significant one-way test with the appropriate post-hoc test (Tukey-Kramer Honestly Significant Difference [HSD] method) in order to determine which pairs of areas differed significantly from each other for each parameter. This statistical design accounted for the family-wise error rate in the MANOVA test and for multiple comparisons in each one-way test and post-hoc tests.

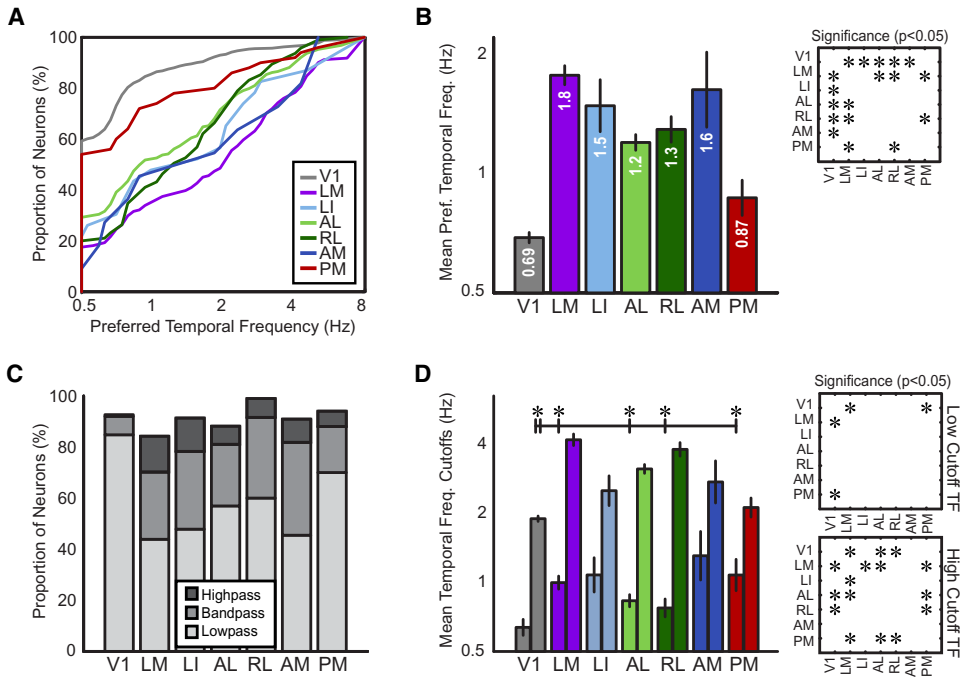

Figure 4. Encoding for Temporal Frequency Information Differs across Visual Areas

(A) Cumulative distributions of preferred temporal frequency (TF) for each visual area (inset color-coding for each area corresponds to all panels).

(B) Geometric mean preferred TF for each visual area.

(C) Proportions of highpass, bandpass, and lowpass neurons for each area.

(D) Geometric mean TF cutoffs show the range of TFs encoded by each population on average. For each area, the left bar indicates the low cutoff TF and the right bar indicates the high cutoff frequency. Asterisks and lines above plot indicate significant differences ($p < 0.05$) between V1's high cutoff frequency and the low cutoff frequency of extrastriate areas.

Insets in (B) and (D) show statistical significance ($p < 0.05$) of pair-wise comparisons between areas, corrected for multiple comparisons using the Tukey-Kramer method. Error bars are standard error of the mean (SEM) in (B) and (D). TF bandwidth comparisons are in Figure S4.

By characterizing responses from large populations of neurons across seven visual areas under the same carefully controlled conditions, we were able to directly compare the statistics of each area's population. The statistical power of this experimental design provides confidence in comparisons made between areas based on combinations of features encoded in each area. As the results presented below indicate, this establishes the basis for the identification of functional specialization of each area investigated.

Extrastriate Visual Areas Encode High Temporal Frequency Information

The geometric means and distributions of preferred TF for each population revealed two groups of areas: one representing low TFs and one representing higher TFs (Figure 4A). The cumulative distributions of preferred TF show that the majority of layer 2/3 neurons in V1 (60%) and PM (54%) responded maximally to the lowest TF we presented (0.5 Hz) and tended to prefer slower frequencies in general, while the populations for all other extrastriate areas were shifted toward faster frequencies (Figure 4A). We compared the geometric mean preferred TF across all areas (Figure 4B), and found a main effect of visual area on preferred TF (one-way ANOVA $F_{(6,1180)} = 49.958$, $p < 0.0005$). We followed up with post-hoc multiple comparisons tests to determine which areas were different from each other in terms of preferred TF. All extrastriate visual areas investigated except area PM had higher preferred TF tuning than V1 (LM, LI, AL, RL, AM; $p < 0.05$, HSD; Figure 4B inset). We also found differences between several extrastriate areas, and these results are summarized in Figure 4B (inset). Area LM had the highest mean preferred TF tuning (significantly higher than areas V1, PM, AL, and RL, $p < 0.05$, HSD).

Neurons were characterized as lowpass, highpass or bandpass for TF (Figure 4C, see Supplemental Experimental Procedures). The great majority of V1 neurons were lowpass for TF and responded higher than 50% maximal to the lowest frequency tested (0.5 Hz). All other areas had larger fractions of bandpass and highpass cells, indicating that the neurons' tuning curves were shifted to higher TFs compared to V1 (Figure 4C). To determine the range of TFs represented by neurons in each population, we examined TF cutoffs (Figure 4D), the stimulus frequencies at which the response decayed to half the maximal response, for each neuron (Heimel et al., 2005). Mean low cutoffs were similar across areas, with only areas LM and PM having statistically higher low cutoff frequencies compared to V1 (Figure 4D, one-way ANOVA, $F_{(6,251)} = 2.89$, $p < 0.01$; post-hoc comparisons $p < 0.05$, HSD). High cutoff frequencies were more variable across areas (one-way ANOVA,

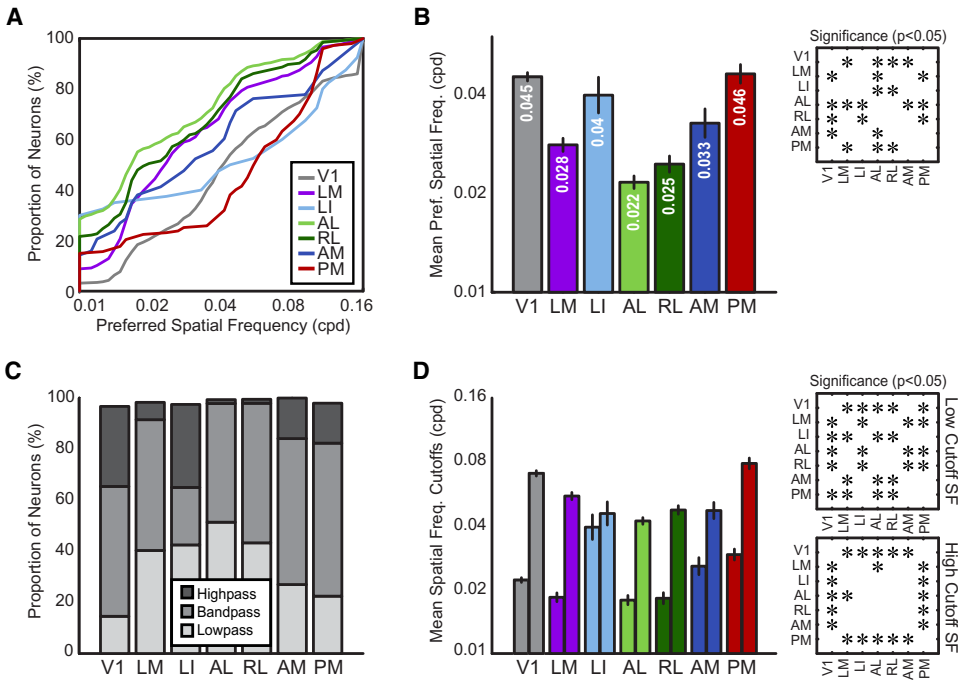

Figure 5. Encoding for Spatial Frequency Information Differs across Visual Areas

(A) Cumulative distributions of preferred spatial frequency (SF) for each visual area.

(B) Geometric mean preferred SF for each area.

(C) Visual areas differ in the proportions of highpass, bandpass, and lowpass neurons across each population.

(D) Geometric mean SF cutoffs across visual areas. For each area, left bar indicates the low cutoff SF and the right bar indicates the high cutoff SF.

Insets in (B) and (D) show statistical significance ($p < 0.05$) of pair-wise comparisons between areas, corrected for multiple comparisons using the Tukey-Kramer method. Error bars are SEM in (B) and D). SF bandwidth comparisons are in Figure S5.

$F_{(6,1013)} = 45.36$, $p < 0.0005$), with areas LM, AL, and RL demonstrating higher high cutoff values than V1.

Given the substantially higher preferred TF tuning of extrastriate visual areas (up to three times the mean tuning of V1), we asked whether the range of TFs encoded by the V1 layer 2/3 population overlapped with that of extrastriate areas to determine whether V1 could provide a source of fast frequency information to higher visual areas. We compared the high cutoff TFs of V1 to the low cutoff TFs of all the extrastriate visual areas investigated. We found that V1's mean high cutoff was significantly higher than the mean low cutoff frequencies for all extrastriate areas except LI and AM (Figure 4D, $p < 0.05$ indicated on graph). These results indicate that V1 encodes TF information that overlaps with the information encoded in areas LM, AL, RL, and PM on average, and thus could supply information within this range to higher visual areas. The distribution of preferred TF preferences in V1 reveals that a small subset of V1 neurons prefer high TFs (Figure 4A), and thus could convey higher TF information to extrastriate areas. Still, V1 has essentially no cells that are highpass for TF, while all extrastriate areas have subsets of cells that respond robustly to the highest TFs tested, indicating that they may prefer higher frequencies than we sampled. This suggests that these neurons cannot simply inherit high temporal frequency tuning from the population we characterized in V1. Encoding for fast frequency information in higher areas could emerge from input from other areas (e.g., lateral posterior nucleus of the thalamus; Simmons et al., 1982), other populations within V1 (e.g., deeper cortical layers; Gao et al., 2010; Kreile et al., 2011), or local circuits.

To address the sharpness of TF tuning across areas, we examined tuning bandwidth. A bandwidth value was computed for bandpass cells as the half width at half max in octaves (Heimel et al., 2005; Figure S4). All extrastriate areas had higher mean TF bandwidth values than V1. This effect was significant for areas LM, AL, and RL (Figure S4, one-way ANOVA $F_{(6,191)} = 5.2$, $p < 0.005$; post-hoc comparisons $p < 0.05$, HSD), and indicates that these areas tend to respond to a broader range of TFs than V1.

A Subset of Extrastriate Areas Encode High Spatial Frequencies

The cumulative distributions of preferred SF for each area's population of neurons showed that all of the visual areas had populations encoding the spectrum of SFs tested. One group of areas—AL, RL, and LM—consisted of neurons preferring relatively low SFs (Figure 5A). Area AM contained neurons which preferred intermediate SFs, and areas V1, LI, and PM all showed high SF tuning. Areas LI and PM show particularly interesting distributions. LI contains a relatively large subset of neurons that prefer the lowest SF, similar to area AL. However, the remaining distribution deviates toward high SFs, suggesting the presence of separate populations of neurons in LI, preferring

distinct ranges of SFs (Figure 5A, Figure S6). Area PM's distribution also has an interesting pattern, with a small population of neurons preferring low SFs which deviates rapidly toward a larger population preferring high SFs (Figure 5A, Figure S6).

We compared the geometric mean preferred SF across each population (Figure 5B) and found a main effect of visual area on preferred SF (one-way ANOVA, $F_{(6,1783)} = 59.7576$, $p < 0.0005$). Post-hoc multiple comparisons tests revealed that areas LM, AL, RL, and AM all prefer lower SFs than V1 (Figure 5B, $p < 0.05$, HSD), while areas LI and PM cannot be distinguished from V1 based on mean preferred SF. Area AL had the lowest preferred SF, significantly lower than areas V1, LM, LI, AM, and PM (Figure 5B, $p < 0.05$, HSD). Only area RL showed comparably low preferred SF. Areas LM and AM showed similar, intermediate preferred SF (Figure 5B).

In the same manner as for TF tuning, we characterized neurons as lowpass, highpass or bandpass for SF (Figure 5C). Areas LM, LI, AL, and RL all had relatively high proportions of neurons which were lowpass, however the populations of neurons from these areas differed in other respects. While areas AL and RL had populations which otherwise consisted of bandpass cells, indicating that we had fully sampled the SF range of the population with our stimuli, areas AM, PM and most notably LI had relatively large fractions of neurons which were highpass. Interestingly, LI contains two distinct populations of either highpass or lowpass cells, with relatively few bandpass cells, which may help explain the similarity in the high and low cutoffs observed for this area (Figure 5D). All areas except AM have significantly different low cutoff values than V1. This effect was toward lower values in all areas except areas LI and PM, which had a higher mean low cutoff than V1 (Figure 5D, one-way ANOVA, $F_{(6,1205)} = 9.91$, $p < 0.0005$; post-hoc comparisons $p < 0.05$, HSD). Visual areas could also be distinguished in terms of SF high cutoffs (Figure 5D). All extrastriate areas had significantly lower mean high cutoff than V1, with the exception of PM, which had a slightly higher mean cutoff than V1, but this effect was not found to be significant. Comparing across extrastriate areas showed that high cutoff SFs were similar for all higher visual areas, except LM, which had a significantly higher mean high cutoff than area AL (Figure 5D, one-way ANOVA, $F_{(6,1445)} = 27.55$, $p < 0.0005$; post-hoc comparisons $p < 0.05$, HSD).

Tuning bandwidth for SF was sharper in all extrastriate areas compared to V1, except area LI (Figure S5, one-way ANOVA $F_{(6,903)} = 15.23$, $p < 0.0005$; post-hoc comparisons $p < 0.05$, HSD). Area LM had significantly broader SF tuning than extrastriate areas AL, RL, and AM (Figure S5, $p < 0.05$, HSD). Area AM had the sharpest spatial frequency tuning bandwidth. These results demonstrate that extrastriate visual areas are more selective for SF than V1.

Extrastriate Visual Areas Are Highly Selective for Orientation and a Subset Are Highly Selective for Direction

We calculated the orientation selectivity index (OSI) at the optimal SF for each neuron (Experimental Procedures). A clear separation could be seen between the cumulative distributions of area V1 compared to all other areas, with the distributions of all extrastriate areas shifted toward higher OSI values (Figure 6A). Population distributions in areas PM, AL, RL, and especially AM stand out as particularly well tuned for orientation relative to the other areas (Figure 6A).

All extrastriate areas except area LI had significantly higher mean OSI values than V1 (Figure 6B, one-way ANOVA $F_{(6,1783)} = 41.74$, $p < 0.0005$; post-hoc comparisons $p < 0.05$, HSD). A subset of areas stood out above the rest: AL, RL, and especially area AM had higher mean OSI values than all other areas, except area PM, which was only significantly lower than area AM (Figure 6B, $p < 0.05$, HSD). AM showed the highest OSI of any of the areas, with significantly higher tuning than all areas except AL (Figure 6B, $p < 0.05$, HSD). These results were also reflected in the proportion of cells that were highly orientation selective (OSI > 0.5, Figure 6C). All extrastriate areas had a larger proportion of highly orientation selective cells than V1, with AL, RL, AM, and PM having the largest proportions of highly selective cells.

We calculated the direction selectivity index (DSI) at the optimal SF for each neuron. Two groups of areas are apparent in the cumulative distributions across areas (Figure 6D). Area LM's, LI's, and PM's distributions closely overlap with V1's distribution, while areas AL, RL, and AM overlap each other and are shifted toward higher DSI (Figure 6D). This distinction is well demonstrated by the mean DSI of each area. Areas AL, RL, and AM had significantly higher mean DSI than areas V1 and LM (Figure 6E, one-way ANOVA, $F_{(6,1783)} = 10.45$, $p < 0.0005$; post-hoc comparisons $p < 0.05$, HSD). Similarly, this group of areas had a larger proportion of highly direction selective neurons with DSI > 0.5 (Figure 6F).

Mouse Visual Areas Encode Distinct Combinations of Spatiotemporal Information

The statistics comparing areas along each tuning metric can be evaluated between pairs of metrics to reveal different combinations of features encoded across areas and to investigate correlations in the coding for pairs of features. We present each combination of preferred SF, preferred TF, OSI, and DSI in Figure 7 as the mean and standard error of each tuning metric versus another for each area. Direct statistical comparisons between areas for each metric are described above and shown in Figures 4–6. In Figure S6 we perform formal correlation analyses between each pair of metrics on a cell-by-cell population basis to determine whether linear relationships exist between pairs of stimulus parameters on the level of encoding in single neurons. In Figure 8 we summarize the mean tuning metrics for each area, intended as a synopsis of the main findings of the paper.

Two main questions about the data can be addressed with these analyses: (1) do combinations of feature representations further distinguish areas from each other, beyond the tuning for any one metric, and (2) do relationships exist between the tuning for particular stimulus parameters?

In reference to the first question, differences between areas are revealed by coding across multiple stimulus parameters. For instance, while areas LM, LI, and AM have statistically similar preferred TF tuning (Figure 4B), area AM can be distinguished from the other two areas as having higher OSI and DSI (Figures

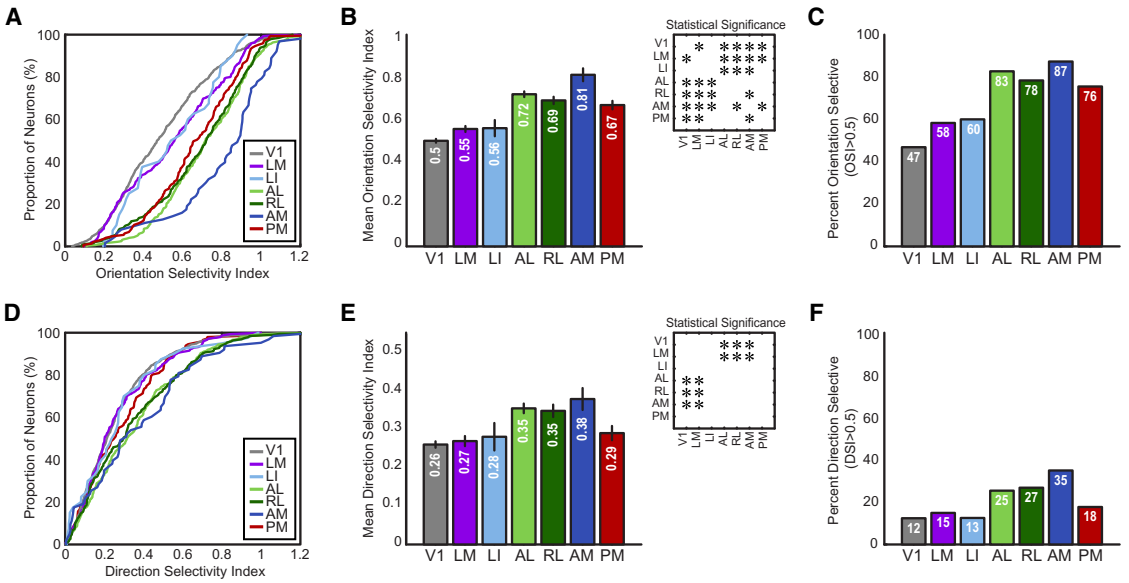

Figure 6. Encoding for Orientation and Direction Information Differs across Visual Areas

(A) Cumulative distributions of orientation selectivity index (OSI) for each area.

(B) Mean OSI for each visual area.

(C) Percent of highly orientation selective neurons (OSI > 0.5) across the population for each area.

(D) Cumulative distributions of direction selectivity index (DSI) for the population of neurons in each visual area.

(E) Mean DSI for each visual area.

(F) Percent of highly direction selective neurons (DSI > 0.5) across the population for each visual area.

Insets in (B) and (E) show statistical significance ($p < 0.05$) of pair-wise comparisons between areas, corrected for multiple comparisons using the Tukey-Kramer method. Error bars are SEM in (B) and (D).

7C, 7D, 6B, and 6E). It is also apparent that V1 can be distinguished from extrastriate areas based on several parameters. Areas AL, RL, and AM are significantly different from V1 across all stimulus dimensions, having higher mean preferred TF, lower mean preferred SF and higher orientation and direction selectivity (Figures 7, 4B, 5B, 6B, and 6E). These relationships also distinguish LM from V1, except in terms of direction selectivity (Figures 7, 4B, 5B, and 6B). Higher orientation selectivity distinguishes PM from V1 (Figure 6B) and higher preferred TF distinguishes LI from V1 (Figure 4B).

With few exceptions, each extrastriate area could be distinguished from all other extrastriate areas based on its combination of mean preferred SF, preferred TF, OSI, and/or DSI. Areas PM and LM were different from LI only in terms of mean SF and/or TF cutoffs (Figures 4D and 5D). Only areas AL and RL were statistically indistinguishable from each other across all mean tuning metrics. A formal comparison of the proportion of responsive cells in each area revealed statistical differences between AL and RL ($\chi^2 = 31.535$, 1 degree of freedom, $p < 0.0001$ for TF proportion, $\chi^2 = 5.047$, 1 degree of freedom, $p < 0.05$ for SF proportion). These results demonstrate that the mouse visual areas investigated in this study are functionally distinct and are specialized to represent different spatiotemporal information.

In terms of general trends in encoding combinations of visual features, some relationships were evident in the mean tuning across visual areas and in cell-by-cell population correlations of each visual area. In most cases, significant correlations in the populations of individual neurons were generally low (generally less than or equal to R = 0.3, Figure S6). This seemed to indicate that populations of neurons in each area were more or less evenly distributed in terms of tuning for pairs of stimulus parameters. Still, some trends were observed, and they may be informative in understanding relationships between tuning for different stimulus parameters. For example, orientation and direction selectivity appear closely related across areas in terms of mean OSI and DSI and are positively correlated in terms of cell-by-cell correlations in areas V1 and LM (Figure 7B and Figure S6B). Areas that prefer high SFs tend to prefer low TFs, except for areas AM and especially LI, which have particularly high mean preferences for both (Figure 7A). Area LI is the only area with a strong negative correlation between SF and TF tuning on a population level ($R = -0.77$, $p < 0.05$, Bonferroni corrected), suggesting that neurons in this area tend to either encode high TFs or high SFs, but not the combination of both (Figure S6A). Areas with high mean preferred TF tend to have higher mean OSI and DSI (Figures 7C and 7D). Positive correlations between these metrics were found for areas V1 and AL for OSI and areas V1, LM, AL, and RL for DSI across each population of neurons (Figures S6C and S6D). The relationships between SF tuning and orientation and direction selectivity are most apparent in cell-by-cell correlations, which show positive correlations between preferred SF and OSI in areas V1, LM, and AL (Figure S6E). SF and DSI are negatively correlated in areas AL, RL, and PM and weakly positively correlated in V1 (Figure S6F).

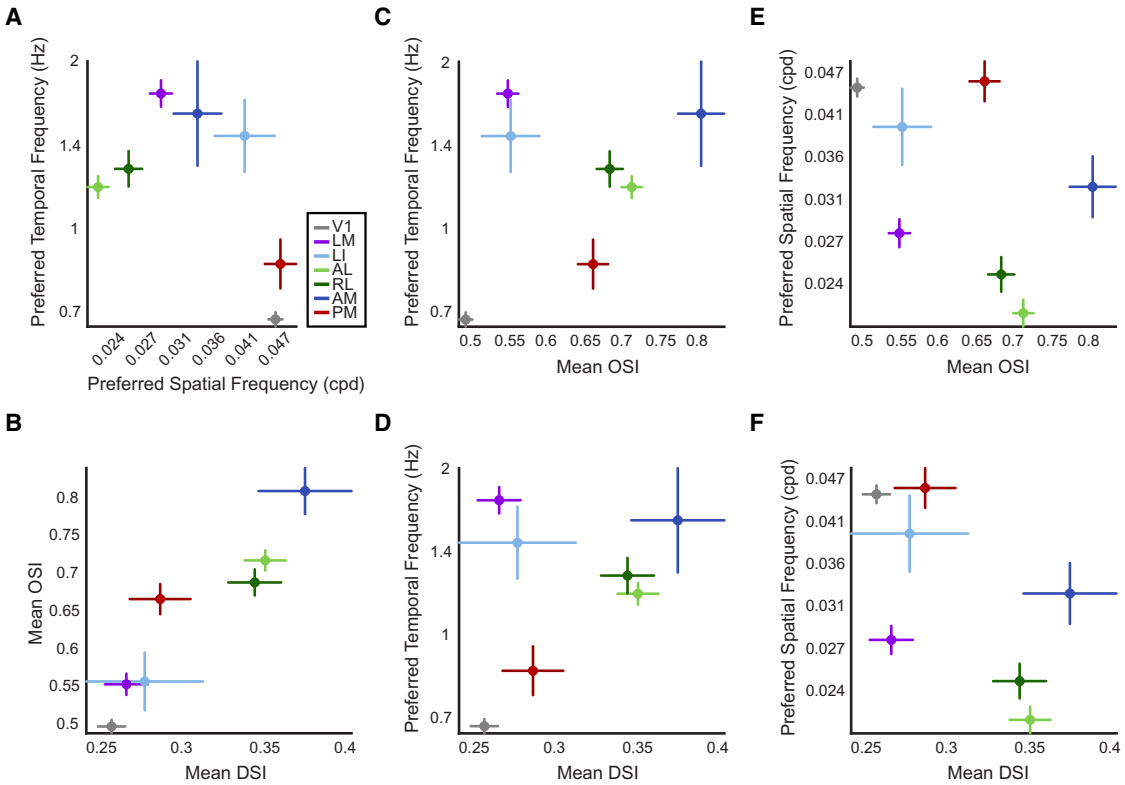

Figure 7. Mouse Cortical Visual Areas Encode Unique Combinations of Spatiotemporal Information

(A–F) Pair-wise combinations between mean preferred temporal frequency, preferred spatial frequency, OSI, and DSI as a function of visual area. For all plots, each point represents the population means of a single visual area for the combination of tuning metrics indicated on the respective axes. Lines extending from each point define an area's SEM for the tuning metric defined on the parallel axis. Statistical comparisons between areas for each metric are same as insets in Figures 4B, 5B, 6B, and 6E. See cell-by-cell population correlations for each metric for each area in Figure S6.

DISCUSSION

In the present study, we found that mouse visual cortex contains a highly organized arrangement of distinct visual areas, which each encode unique combinations of spatiotemporal features. Our nearly complete, high-resolution retinotopic maps reveal a continuous fine-scale organization across mouse visual cortex, comprising at least nine independent representations of the contralateral visual field. As was previously shown for mouse V1 (Niell and Stryker, 2008) and similar to what has been found in other species (Felleman and Van Essen, 1987; Orban, 2008; Payne, 1993), each of the six mouse extrastriate visual areas we investigated contains neurons that are highly selective for fundamental visual features, including orientation, direction, spatial frequency (SF), and temporal frequency (TF). All extrastriate areas investigated, with the exception of PM, encode faster TFs than V1, suggesting a role for these higher areas in the processing of visual motion. For a subset of areas, AL, RL, and AM, this role is further supported by a significant increase in direction selectivity across each population. Another subset of areas, LI and PM, prefer high SFs, suggesting a role in the processing of structural detail in an image. Nearly all higher visual areas improve orientation selectivity compared to V1.

Every visual area could be distinguished from every other visual area statistically by comparing scores on multiple tuning metrics (and AL from RL based on fraction of responsive neurons), indicating functional specialization of spatiotemporal information processing across mouse visual areas. The combination of distinct retinotopic representations and functionally specialized neuronal populations establish that mouse visual cortex is composed of several discrete visual areas that each encode unique combinations of visual features. These findings reveal that the mouse visual system shares fundamental organizational principles with other species and is more highly developed than expected from previous work focusing almost exclusively on V1. Future studies examining selectivity for more complex stimuli under different behavioral conditions may reveal additional specializations of each visual area.

Striking similarities are evident among subsets of extrastriate areas along specific feature dimensions. These complex relationships likely reflect underlying rules of connectivity that link processing between certain areas, and may relate to the grouping of areas into hierarchically organized parallel pathways. Areas AL, RL, and AM are all highly direction selective and respond to high TFs and low SFs. These properties have served as hallmarks of the dorsal pathway in other species (Maunsell and Newsome, 1987; Nassi and Callaway, 2009; Van

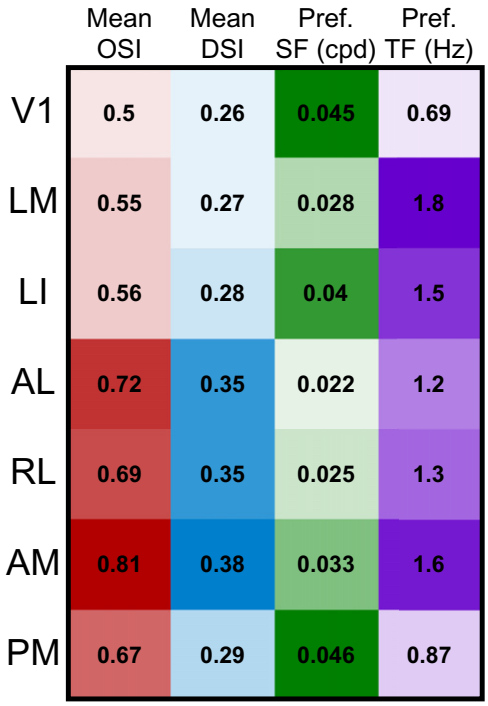

Figure 8. Summary of Feature Selectivities across Seven Mouse Visual Areas

Mean values for orientation selectivity, direction selectivity, preferred spatial frequency and preferred temporal frequency for each area, corresponding to results depicted in Figures 4–7, summarized together here to illustrate the specific combinations of spatial and temporal features encoded by each area. Color intensity represents the magnitude of each parameter relative to the lowest and highest values across all areas, with higher values indicated by darker colors. Comparison of tuning for multiple stimulus parameters reveals the unique combination of spatiotemporal information represented by each area and highlights the similarities and differences across areas.

Essen and Gallant, 1994) and suggest that AL, RL, and AM perform computations related to the analysis of visual motion. This role is further supported by the anatomical position of these areas in the posterior parietal cortex, which corresponds to the location of dorsal stream areas in other species and is closely related to neural systems for spatial navigation and motor output (Kaas et al., 2011; Kravitz et al., 2011; Ungerleider and Mishkin, 1982). In contrast, areas LI and PM respond to high SFs, and PM is highly orientation selective, suggesting a role in the analysis of structural detail and form in an image (Desimone et al., 1985; Maunsell and Newsome, 1987). These results suggest that the mouse visual cortex may be organized into groups of specialized areas that process information related to motion and behavioral actions versus image detail and object perception, analogous to the dorsal and ventral streams described in other species.

Defining hierarchical relationships in mouse visual cortex and conclusively relating specific areas to dorsal and ventral streams will require significant future behavioral, anatomical and functional work. Rodents can perform spatial and pattern discrimination tasks (Douglas et al., 2006; Prusky and Douglas, 2004; Sánchez et al., 1997; Wong and Brown, 2006), similar to those shown to depend on dorsal and ventral pathways in higher species (Mishkin et al., 1983). However, little is known about how specific mouse visual areas or pathways relate to these behaviors. Recently, it was found that AL and LM afferents differentially target brain regions typically associated with the dorsal and ventral pathways (Wang et al., 2011). These anatomical distinctions led to the suggestion that LM and AL belong to the ventral and dorsal streams respectively. The results of our functional imaging study support the role of areas AL, RL, and AM in dorsal-like motion computations and of LI and PM in ventral-like spatial computations. However, our results are less conclusive for area LM's role in ventral-like computations. It encodes the highest TFs in our data set and prefers moderate SFs—properties typically associated with the dorsal stream in other species (Van Essen and Gallant, 1994). In addition to behavioral and anatomical data, examining selectivity of higher visual areas to more complex stimuli can further illuminate the higher-order computations they perform and their relationships to information processing streams (Maunsell and Newsome, 1987).

While our data indicate that mouse visual cortex shares general organizational principles with other species, several important distinctions can be made. One major difference between the rodent visual cortex and primate visual cortex is the existence of direct V1 input to essentially all extrastriate visual areas in the mouse and rat (Coogan and Burkhalter, 1993; Olavarria and Montero, 1989; Wang and Burkhalter, 2007), whereas only areas V2, V3, V4, and MT are known to receive substantial direct V1 input in the primate brain (Felleman and Van Essen, 1991). Differences in the function and organization of visual areas between mice and other species are likely related to specializations resulting from species-specific behavioral adaptations. While multimodal interactions are typically associated with select higher-level areas in primates (Felleman and Van Essen, 1991; Ungerleider and Mishkin, 1982), there is evidence that several rodent extrastriate areas process information related to other sensory modalities (Miller and Vogt, 1984; Sanderson et al., 1991; Wagor et al., 1980). This may indicate fewer hierarchical stages in the rodent, relating visual information more readily to multimodal interactions or complex behaviors such as spatial navigation. The extent to which mouse visual pathways resemble dorsal and ventral streams and are organized into hierarchical pathways, as well as understanding the role of specific areas in perception and behavior, form the basis for useful, testable hypotheses for future investigation.

Implications for Motion Processing in Mouse Extrastriate Cortex

Our population analyses revealed prominent differences in the tuning for motion-related visual features between several extrastriate areas and V1. V1 neurons generally prefer low TFs, theoretically making it difficult for V1 neurons to resolve stimulus motion beyond low velocities. On the other hand, all mouse extrastriate visual areas except PM prefer high TFs relative to V1. Some extrastriate areas, notably areas LM, AM, and LI, prefer TFs two to three times the rate of V1 on average, and areas AL and RL prefer frequencies almost double that of V1.

Furthermore, areas AL, RL, and AM contain a larger proportion of highly direction selective neurons, and are significantly more direction selective on average compared to V1 and LM. These findings demonstrate that mouse extrastriate visual areas, especially AL, RL, and AM, are better suited to process motion information than V1. Intriguingly, these areas compose part of the posterior parietal cortex, which has been implicated in spatial discrimination and navigation tasks in rats and is involved in similar behaviors as part of the dorsal pathway in primates (Kravitz et al., 2011; Ungerleider and Mishkin, 1982; Whitlock et al., 2008). The ability of neurons in these areas to encode changes in a stimulus at fast frequencies suggests that they can follow high velocities through their receptive fields. Determining whether each extrastriate area we examined encodes motion information per se, or rather encodes high temporal resolution to serve higher-order motion computations in other areas requires future studies. For example, in addition to having high direction selectivity, neurons in the motion-selective middle temporal area (MT) in primates represent higher-order features such as speed and pattern motion (Maunsell and Newsome, 1987).

Encoding Spatial Detail in Mouse Visual Cortex

The mouse visual system, while modest in acuity compared to primates and many carnivore species, is capable of spatial discrimination across several orders of spatial magnitude (Prusky and Douglas, 2004) and is known to contain neurons that are highly selective for SF and spatial details such as orientation in primary visual cortex and to some extent subcortical structures (Grubb and Thompson, 2003; Niell and Stryker, 2008; Wang et al., 2010). In the present study we found that extrastriate areas LI and PM prefer SFs comparable to the relatively high frequencies represented in V1. Additionally, all extrastriate visual areas except perhaps LI are more sharply tuned for SF and are more selective for orientation than V1. These findings imply that a subset of extrastriate visual areas, including LI and PM, are capable of conveying high spatial resolution details in an image, and in the case of area PM, actually improve the fidelity of these responses in terms of SF bandwidth and higher selectivity for orientation (higher than both V1 and LM). Tuning for high SFs and good orientation selectivity are attributed to the ventral pathway in primates, ultimately leading to object perception (Maunsell and Newsome, 1987; Van Essen and Gallant, 1994). This suggests that area PM, and to some extent LI, may perform similar computations within the mouse visual system.

Implications for Future Studies

The circuit mechanisms that facilitate computation of fast frequency information, increased direction selectivity, and high spatial frequency preference in different subsets of extrastriate visual areas remain unclear. Selective response properties in extrastriate visual areas could be inherited from lower areas (e.g., V1) based on selective connectivity. Higher-order computations performed across hierarchical levels via specific connections could also help explain the observed patterns of selectivity. Additionally, local computations within each area could sharpen orientation selectivity (Liu et al., 2011) or SF bandwidth tuning via local circuit interneurons. Extrastriate areas could also receive selective information through alternate pathways, such as via projections from the superior colliculus through the lateral posterior nucleus of the thalamus, bypassing V1 entirely (Sanderson et al., 1991; Simmons et al., 1982). A similar pathway exists between the analogous pulvinar nucleus and extrastriate areas in the primate (Lyon et al., 2010). Finally, given that we sampled exclusively from layer 2/3 neurons, the possibility remains that information is conveyed via deeper layers in V1, perhaps bypassing the typical layer 4 → layer 2/3 cortical circuit. Indeed, such circuitry has been demonstrated anatomically in the primate between V1 deep layers and area MT (Nassi et al., 2006; Nhan and Callaway, 2012). Future studies directly examining the relationships between function and connectivity are necessary to understand how visual areas derive their response properties. The mouse model provides powerful tools to address these issues.

Understanding the mechanisms by which information is routed in the cortex requires methods to simultaneously examine both the functional roles of specific cells, circuits, and areas and their patterns of connections with each of these component levels of the network. Further, in order to obtain a complete picture of these interactions and establish causal relationships, techniques allowing controlled, reversible activation and inactivation of targeted circuit elements are necessary. Combining molecular, genetic and viral methods for identifying, targeting and manipulating specific genes, cell types and connections with advanced recording and imaging technologies will make these types of experiments possible. Studies utilizing these technologies have already contributed to an increased understanding of network function in many systems. Currently, these tools are most readily applicable in the mouse, due to its genetic accessibility and small size. Importantly, the small lissencephalic cortex of the mouse permits access to all cortical regions exposed on its flat surface, and deep cortical layers to be analyzed with two-photon imaging (Osakada et al., 2011). While these methods may eventually be applied in other, larger species such as the primate, large-scale studies involving many animals will remain difficult. As such, the mouse will prove an invaluable system for the study of cortical information processing.

The present study provides a thorough characterization of the function of the majority of mouse extrastriate visual areas, demonstrating specialized information processing in seven retinotopically identified visual areas. These results suggest that several high-order computations may occur in mouse extrastriate cortex, and that the mouse visual system shares many of the complexities of the primate system, including well organized, retinotopically defined visual areas and highly selective, specialized neuronal populations, perhaps organized into specific parallel pathways. Furthermore, this study develops and demonstrates several methodological approaches to efficiently investigate several visual areas in the same animal, and across multiple animals in a high-throughput fashion. The results and implications of the current study, as well as the development and application of technologies, lay the foundation for future studies investigating the complexities of the mouse cortical system to reveal circuit-level mechanisms driving high-order computations.

EXPERIMENTAL PROCEDURES

Animal Preparation and Surgery

All experiments involving living animals were approved by the Salk Institute's Institutional Animal Care and Use Committee. C57BL/6 mice (n = 28) between 2 and 3 months were anesthetized with isoflurane (2%–2.5% induction, 1%–1.25% surgery). Dexamethasone and carprofen were administered subcutaneously (2 mg/kg and 5 mg/kg respectively), and ibuprofen (30 mg/kg) was administered postoperatively if the animal recovered overnight after implanting the recording chamber. A custom-made metal frame was mounted to the skull and the bone was thinned over visual cortex for intrinsic imaging, and a craniotomy was made for calcium imaging. After surgery, chlorprothixene (2.5 mg/kg) was administered intramuscularly and isoflurane was reduced to 0.25%–0.8% for visual stimulation and recording experiments.

Intrinsic Signal and Two-Photon Imaging

Intrinsic signal imaging was adapted from previous studies (Kalatsky and Stryker, 2003; Nauhaus and Ringach, 2007). Retinotopic maps from intrinsic signal imaging experiments were used to target locations of Oregon Green Bapta-1 AM and sulforhoadamine-101 loading. Two-photon imaging was performed at ~130–180 μm below the dura surface (layer 2/3).

Visual Stimulation

Drifting bar and drifting grating stimuli were displayed on a gamma-corrected, large LCD display. The screen was oriented parallel to the eye and placed 10 cm from the animal (to stimulate 153° vertical by 147° horizontal). For retinotopy experiments, a bar stimulus (20° × 155°) drifted 10 times along each cardinal axis. Spherical correction was applied to the stimulus to define eccentricity in spherical coordinates (Figure S1, Movies S1 and S2, Supplemental Experimental Procedures).

For drifting grating experiments, spherical altitude correction was applied to sinusoidal gratings to hold SF and TF constant throughout the visual field (Figure S1, Movies S1 and S2, Supplemental Experimental Procedures). For each population of neurons (a single 40× imaging plane), we presented four sets of stimuli: a temporal frequency (TF) varying experiment (0.5, 1, 2, 4, and 8 Hz, 8 directions plus blank, ~0.04 cpd, 5 repeats pseudorandomized for each parameter combination), a spatial frequency (SF) varying experiment (0.01, 0.02, 0.04, 0.08, and 0.16 cpd, 8 directions plus blank, ~1 Hz, 5 repeats pseudorandomized for each parameter combination), a 12 direction orientation tuning experiment (~1 Hz, ~0.04 cpd, 5 repeats pseudorandomized for each parameter combination and a blank condition), and a drifting bar retinotopy experiment (stimulus as described above). A gray screen (mean luminance of grating stimuli) was shown between trials and during the prestimulus baseline period (1 s). Stimulus durations were 4 s for the TF experiment and 2 s for the SF and 12 direction experiments. Data are not presented for the 12 direction experiments.

Data Analysis

Retinotopic maps from intrinsic signal imaging were computed as previously described (Kalatsky and Stryker, 2003). A comparable approach was used to compute retinotopy in Ca^{2+} imaging experiments.

For cellular imaging analysis, movement correction was applied to time-lapse movies and regions of interest (ROIs) were drawn around each cell in the field of view. Glia cells were removed from the analysis using sulforhodamine staining (Nimmerjahn et al., 2004). Pixels were averaged within each ROI for each image frame. Baseline calcium fluorescence was computed for each trial as the mean during the prestimulus period. Then, fluorescence values were converted to percent change above baseline according to the following: $\Delta F/F = (F_I - F)/F$, where F_I is the instantaneous fluorescence signal and F is the baseline fluorescence. The mean ΔF/F was computed over a 2 s window following stimulus onset for each trial, and the mean and standard deviation across trials for each stimulus and blank condition were computed for each neuron.

Neurons were deemed visually responsive if they gave a mean response above 6% ΔF/F to any stimulus. A response reliability metric (δ) was computed for each neuron as follows:

$$\delta = \frac{\mu_{max} - \mu_{blank}}{\sigma_{max} + \sigma_{blank}}$$

where μ_{max} and σ_{max} are the mean and standard deviations of the response to the preferred stimulus respectively, and μ_{blank} and σ_{blank} are the mean and standard deviations of the response to the blank stimulus respectively. Neurons were deemed reliable for $\delta > 1$. Finally, the eccentricity value for each neuron, mapped with the retinotopy stimulus at cellular resolution, was used to restrict our analyses to eccentricity-matched neurons within 50° of the center of space in each area (Table S1). See Supplemental Experimental Procedures for details.

Tuning Metrics and Statistics

SF and TF tuning curves were taken at the optimal orientation and direction for each neuron and orientation and direction tuning curves were taken at the optimal SF for each neuron, using the average ΔF/F response for each condition across trials.

The orientation selectivity index (OSI) was computed as follows:

$$OSI = \frac{\mu_{max} - \mu_{orth}}{\mu_{max} + \mu_{orth}}$$

where μ_{max} is the mean response to the preferred orientation and μ_{orth} is the mean response to the orthogonal orientation (average of both directions). The direction selectivity index (DSI) was computed as follows:

$$DSI = \frac{\mu_{max} - \mu_{opp}}{\mu_{max} + \mu_{opp}}$$

where μ_{max} is the mean response to the preferred direction and μ_{opp} is the mean response to the opposite direction.

Statistical procedures are described in detail in Supplemental Experimental Procedures.

SUPPLEMENTAL INFORMATION

Supplemental Information includes one table, six figures, Supplemental Experimental Procedures, and two movies and can be found with this article online at doi:10.1016/j.neuron.2011.12.004.

ACKNOWLEDGMENTS

We wish to thank the Callaway lab for helpful discussions and technical assistance and K. Nielsen for imaging advice. We acknowledge support from NIH grants EY01742 (EMC), NS069464 (EMC), and EY019821 (IN) and from Gatsby Charitable Foundation and Institute for Neural Computation, UCSD.

Accepted: December 5, 2011
Published: December 21, 2011

REFERENCES

Arenkiel, B.R., and Ehlers, M.D. (2009). Molecular genetics and imaging technologies for circuit-based neuroanatomy. Nature *461*, 900–907.

Baker, J.F., Petersen, S.E., Newsome, W.T., and Allman, J.M. (1981). Visual response properties of neurons in four extrastriate visual areas of the owl monkey (Aotus trivirgatus): a quantitative comparison of medial, dorsomedial, dorsolateral, and middle temporal areas. J. Neurophysiol. *45*, 397–416.

Berezovskii, V.K., Nassi, J.J., and Born, R.T. (2011). Segregation of feedforward and feedback projections in mouse visual cortex. J. Comp. Neurol. *519*, 3672–3683.

Coogan, T.A., and Burkhalter, A. (1993). Hierarchical organization of areas in rat visual cortex. J. Neurosci. *13*, 3749–3772.

Desimone, R., Schein, S.J., Moran, J., and Ungerleider, L.G. (1985). Contour, color and shape analysis beyond the striate cortex. Vision Res. *25*, 441–452.

Douglas, R.M., Neve, A., Quittenbaum, J.P., Alam, N.M., and Prusky, G.T. (2006). Perception of visual motion coherence by rats and mice. Vision Res. *46*, 2842–2847.

Dräger, U.C. (1975). Receptive fields of single cells and topography in mouse visual cortex. J. Comp. Neurol. *160*, 269–290.

Felleman, D.J., and Van Essen, D.C. (1987). Receptive field properties of neurons in area V3 of macaque monkey extrastriate cortex. J. Neurophysiol. *57*, 889–920.

Felleman, D.J., and Van Essen, D.C. (1991). Distributed hierarchical processing in the primate cerebral cortex. Cereb. Cortex *1*, 1–47.

Foster, K.H., Gaska, J.P., Nagler, M., and Pollen, D.A. (1985). Spatial and temporal frequency selectivity of neurones in visual cortical areas V1 and V2 of the macaque monkey. J. Physiol. *365*, 331–363.

Gao, E., DeAngelis, G.C., and Burkhalter, A. (2010). Parallel input channels to mouse primary visual cortex. J. Neurosci. *30*, 5912–5926.

Grubb, M.S., and Thompson, I.D. (2003). Quantitative characterization of visual response properties in the mouse dorsal lateral geniculate nucleus. J. Neurophysiol. *90*, 3594–3607.

Heimel, J.A., Van Hooser, S.D., and Nelson, S.B. (2005). Laminar organization of response properties in primary visual cortex of the gray squirrel (Sciurus carolinensis). J. Neurophysiol. *94*, 3538–3554.

Kaas, J.H., Gharbawie, O.A., and Stepniewska, I. (2011). The organization and evolution of dorsal stream multisensory motor pathways in primates. Front Neuroanat *5*, 34.

Kalatsky, V.A., and Stryker, M.P. (2003). New paradigm for optical imaging: temporally encoded maps of intrinsic signal. Neuron *38*, 529–545.

Kerlin, A.M., Andermann, M.L., Berezovskii, V.K., and Reid, R.C. (2010). Broadly tuned response properties of diverse inhibitory neuron subtypes in mouse visual cortex. Neuron *67*, 858–871.

Kravitz, D.J., Saleem, K.S., Baker, C.I., and Mishkin, M. (2011). A new neural framework for visuospatial processing. Nat. Rev. Neurosci. *12*, 217–230.

Kreile, A.K., Bonhoeffer, T., and Hübener, M. (2011). Altered visual experience induces instructive changes of orientation preference in mouse visual cortex. J. Neurosci. *31*, 13911–13920.

Liu, B.H., Li, Y.T., Ma, W.P., Pan, C.J., Zhang, L.I., and Tao, H.W. (2011). Broad inhibition sharpens orientation selectivity by expanding input dynamic range in mouse simple cells. Neuron *71*, 542–554.

Luo, L., Callaway, E.M., and Svoboda, K. (2008). Genetic dissection of neural circuits. Neuron *57*, 634–660.

Lyon, D.C., Nassi, J.J., and Callaway, E.M. (2010). A disynaptic relay from superior colliculus to dorsal stream visual cortex in macaque monkey. Neuron *65*, 270–279.

Maunsell, J.H., and Newsome, W.T. (1987). Visual processing in monkey extrastriate cortex. Annu. Rev. Neurosci. *10*, 363–401.

Miller, M.W., and Vogt, B.A. (1984). Direct connections of rat visual cortex with sensory, motor, and association cortices. J. Comp. Neurol. *226*, 184–202.

Mishkin, M., Ungerleider, L.G., and Macko, K.A. (1983). Object vision and spatial vision: two cortical pathways. Trends Neurosci. *6*, 414–417.

Nassi, J.J., and Callaway, E.M. (2009). Parallel processing strategies of the primate visual system. Nat. Rev. Neurosci. *10*, 360–372.

Nassi, J.J., Lyon, D.C., and Callaway, E.M. (2006). The parvocellular LGN provides a robust disynaptic input to the visual motion area MT. Neuron *50*, 319–327.

Nauhaus, I., and Ringach, D.L. (2007). Precise alignment of micromachined electrode arrays with V1 functional maps. J. Neurophysiol. *97*, 3781–3789.

Nauhaus, I., Nielsen, K.J., and Callaway, E.M. (2011). Nonlinearity of two-photon Ca2+ imaging yields distorted measurements of tuning for V1 neuronal populations. J. Neurophysiol. Published online November 23, 2011. 10.1152/jn.00725.2011.

Nhan, H.L., and Callaway, E.M. (2012). Morphology of superior colliculus- and middle temporal area-projecting neurons in primate primary visual cortex. J. Comp. Neurol. *520*, 52–80.

Niell, C.M., and Stryker, M.P. (2008). Highly selective receptive fields in mouse visual cortex. J. Neurosci. *28*, 7520–7536.

Nimmerjahn, A., Kirchhoff, F., Kerr, J.N., and Helmchen, F. (2004). Sulforhodamine 101 as a specific marker of astroglia in the neocortex in vivo. Nat. Methods *1*, 31–37.

Olavarria, J., and Montero, V.M. (1989). Organization of visual cortex in the mouse revealed by correlating callosal and striate-extrastriate connections. Vis. Neurosci. *3*, 59–69.

Orban, G.A. (2008). Higher order visual processing in macaque extrastriate cortex. Physiol. Rev. *88*, 59–89.

Osakada, F., Mori, T., Cetin, A.H., Marshel, J.H., Virgen, B., and Callaway, E.M. (2011). New rabies virus variants for monitoring and manipulating activity and gene expression in defined neural circuits. Neuron *71*, 617–631.

Payne, B.R. (1993). Evidence for visual cortical area homologs in cat and macaque monkey. Cereb. Cortex *3*, 1–25.

Polimeni, J.R., Granquist-Fraser, D., Wood, R.J., and Schwartz, E.L. (2005). Physical limits to spatial resolution of optical recording: clarifying the spatial structure of cortical hypercolumns. Proc. Natl. Acad. Sci. USA *102*, 4158–4163.

Prusky, G.T., and Douglas, R.M. (2004). Characterization of mouse cortical spatial vision. Vision Res. *44*, 3411–3418.

Sánchez, R.F., Montero, V.M., Espinoza, S.G., Díaz, E., Canitrot, M., and Pinto-Hamuy, T. (1997). Visuospatial discrimination deficit in rats after ibotenate lesions in anteromedial visual cortex. Physiol. Behav. *62*, 989–994.

Sanderson, K.J., Dreher, B., and Gayer, N. (1991). Prosencephalic connections of striate and extrastriate areas of rat visual cortex. Exp. Brain Res. *85*, 324–334.

Schuett, S., Bonhoeffer, T., and Hübener, M. (2002). Mapping retinotopic structure in mouse visual cortex with optical imaging. J. Neurosci. *22*, 6549–6559.

Sereno, M.I., Dale, A.M., Reppas, J.B., Kwong, K.K., Belliveau, J.W., Brady, T.J., Rosen, B.R., and Tootell, R.B. (1995). Borders of multiple visual areas in humans revealed by functional magnetic resonance imaging. Science *268*, 889–893.

Simmons, P.A., Lemmon, V., and Pearlman, A.L. (1982). Afferent and efferent connections of the striate and extrastriate visual cortex of the normal and reeler mouse. J. Comp. Neurol. *211*, 295–308.

Tohmi, M., Takahashi, K., Kubota, Y., Hishida, R., and Shibuki, K. (2009). Transcranial flavoprotein fluorescence imaging of mouse cortical activity and plasticity. J. Neurochem. *109* (*Suppl 1*), 3–9.

Ungerleider, L.G., and Mishkin, M. (1982). Two cortical visual systems. In Analysis of Visual Behavior, D.J. Ingle, M.A. Goodale, and R.J.W. Mansfield, eds. (Cambridge, MA: MIT Press), pp. 549–586.

Van den Bergh, G., Zhang, B., Arckens, L., and Chino, Y.M. (2010). Receptive-field properties of V1 and V2 neurons in mice and macaque monkeys. J. Comp. Neurol. *518*, 2051–2070.

Van Essen, D.C. (2003). Organization of visual areas in macaque and human cerebral cortex. In The Visual Neurosciences, L. Chalupa, ed. (Cambridge, MA: MIT Press).

Van Essen, D.C., and Gallant, J.L. (1994). Neural mechanisms of form and motion processing in the primate visual system. Neuron *13*, 1–10.

Wagor, E., Mangini, N.J., and Pearlman, A.L. (1980). Retinotopic organization of striate and extrastriate visual cortex in the mouse. J. Comp. Neurol. *193*, 187–202.

Wang, Q., and Burkhalter, A. (2007). Area map of mouse visual cortex. J. Comp. Neurol. *502*, 339–357.

Wang, L., Sarnaik, R., Rangarajan, K., Liu, X., and Cang, J. (2010). Visual receptive field properties of neurons in the superficial superior colliculus of the mouse. J. Neurosci. *30*, 16573–16584.

Wang, Q., Gao, E., and Burkhalter, A. (2011). Gateways of ventral and dorsal streams in mouse visual cortex. J. Neurosci. *31*, 1905–1918.

Whitlock, J.R., Sutherland, R.J., Witter, M.P., Moser, M.B., and Moser, E.I. (2008). Navigating from hippocampus to parietal cortex. Proc. Natl. Acad. Sci. USA *105*, 14755–14762.

Wong, A.A., and Brown, R.E. (2006). Visual detection, pattern discrimination and visual acuity in 14 strains of mice. Genes Brain Behav. *5*, 389–403.